Author: Velliscig, Marco
Title: Probing the darkness : the link between baryons and dark matter
Issue Date: 2015-11-11

5

Galaxy-Galaxy Lensing in EAGLE: comparison with data from 100 square degrees of the KiDS and GAMA surveys

We present predictions for the galaxy-galaxy lensing (GGL) profile from the EAGLE hydrodynamical cosmological simulation. These predictions are computed at redshift zero, in the spatial range $-1.7 < \log_{10}[r_p/(h^{-1}\mathrm{Mpc})] < 0.3$, and for 6 logarithmically equispaced stellar mass bins in the range $10 < \log_{10}(M_{\mathrm{star}}[\mathrm{M}_\odot]) < 11.8$. We compare them with the observed signal measured using background galaxies imaged by the KiDS survey around spectroscopically confirmed foreground galaxies from the GAMA survey. Overall, the predicted lensing signal is in broad agreement with observations, as expected from the fact that the EAGLE simulation has been calibrated to reproduce the redshift zero galaxy stellar mass function. Exploiting the GAMA galaxy group catalogue, the GGL profiles of central and satellite galaxies are also computed independently but this split is limited to groups with at least five members to minimize contamination by false identification. We find good agreement between the EAGLE predictions and the observations for both central and satellite galaxies. When central and satellite galaxies in groups with at least five members are analyzed jointly, predictions result in a poorer agreement with observations. This stems from the fact that the total GGL profile is a linear combination of central and satellite profiles with the satellite fraction as the linear coefficient and that the satellite fraction in the EAGLE simulation is always lower than that in the GAMA group catalogue. The discrepancy in the satellite fraction may, at least partially, originate from the comparison of a flux limited sample (GAMA) to a volume limited one (EAGLE). As the precision of the measurements is about 10%, we find it important to explore the effect of possible systematics in the stacking procedure. Specifically, we focus on two possible sources of error in assigning stellar masses to simulated galaxies. We assume a random error of 0.1 dex to mimic observational uncertainties in inferring stellar masses and we restrict the definition of stellar mass to the sum of masses of star particles within 30 kpc to mimic the observational caveat that stars in a galaxy's outskirts do not enter into the estimation of the galaxy flux. The inclusion of random errors has a very small effect on the GGL profile, whereas considering only stars within 30 kpc increases the estimated ESD profile.

Velliscig, Cacciato, Schaye, Hoekstra

5.1 Introduction

The connection between observable galaxy properties and the underlying (mostly dark) matter density field is the result of galaxy formation and evolution in a cosmological context and as such it is extensively studied from various complementary perspectives. With the advent of large and homogeneous galaxy surveys (e.g. 2dFGRS, SDSS, CFHTLS, KiDS[1]), the link between the stellar content of galaxies and their dark matter halos can be addressed statistically.

Numerous methods are available to probe the mass of dark matter haloes within the galaxy formation framework : galaxy clustering (see e.g. Jing et al. 1998; Peacock & Smith 2000; Zehavi et al. 2002; van den Bosch et al. 2003; Anderson et al. 2014), abundance matching (see e.g. Vale & Ostriker 2004; Moster et al. 2013; Behroozi et al. 2013) and stacked satellite kinematics (see e.g. Zaritsky & White 1994; Prada et al. 2003; Conroy et al. 2005; More et al. 2011). These methods assume, in various ways, a prior knowledge of galaxy formation theory. They are, therefore, limited in their capacity to produce a stellar mass versus halo mass relation that can serve as a test for the galaxy formation framework itself.

For single galaxies, direct methods for estimating the halo mass are available (see for a recent review Courteau et al. 2014). The rotation curves of spiral galaxies or the velocity dispersion of ellipticals can give estimates of total galaxy mass, albeit at relatively small scales. Furthermore, the light of a galaxy can be lensed into multiple images by another galaxy along the line of sight (strong galaxy-galaxy lensing), providing a measurement of the total projected mass within the Einstein radii of galaxies (Kochanek 1991; Bolton et al. 2008; Collett 2015, and references therein). The masses of groups or clusters of galaxies can be estimated via the dynamics of their satellite galaxies (see e.g. Prada et al. 2003; Conroy et al. 2005), using strong lensing (see e.g. Fort & Mellier 1994; Massey et al. 2010) or X-ray emission (Ettori et al. 2013, and references therein).

For a population of galaxies, galaxy-galaxy weak lensing (see e.g. Brainerd et al. 1996; Wilson et al. 2001; Hoekstra et al. 2004; Mandelbaum et al. 2006; van Uitert et al. 2011; Velander et al. 2014; Viola et al. 2015; van Uitert et al. 2015) offers the possibility to measure directly the average halo mass and therefore represents a viable alternative to test galaxy formation models.

Galaxy-galaxy lensing measures the distortion and magnification of the light of faint background galaxies (sources) caused by the deflection of light rays by intervening matter along the line of sight (lenses). The effect is independent of the dynamical state of the lens, and the projected mass of the lens is measured without any assumption on the physical state of the matter. The gravitational lensing signal due to a single galaxy is too weak to be detected (it is typically 10 to 100 times smaller than the true ellipticity of galaxies). Therefore the galaxy-galaxy signal must be averaged over many lenses.

The link between haloes and galaxies can be studied theoretically with an *ab-initio* approach using Semi Analytical Models (SAMs) and hydrodynamical cosmological simulations. Simulations in particular aim at the direct modelling of the physical processes that are thought to be important for the formation of galaxies, as well as the energetic feedback from supernovae and AGN that is thought to regulate their growth (see Somerville & Davé 2014, for a recent review). However, many of these processes are happening on scales that are unresolved by simulations and as such they must be treated as 'subgrid' physics. A key test for such studies is to reproduce the observed abundances of galaxies as a function of their stellar mass (galaxy stellar mass function; hereafter GSMF), as this is interpreted as the achievement of

[1] 2dFGRS: http://www.2dfgrs.net/;
SDSS: http://www.sdss.org/;
KIDS: KIlo-Degree Survey, http://www.astro-wise.org/projects/KIDS/;
CFHTLS: http://www.cfht.hawaii.edu/Science/CFHTLS/

a successful mapping between the stellar mass and the halo mass. However, reproducing the GSMF has proven to be extremely challenging for simulations of galaxy formation. Since most of the radiative losses are due to unresolved physics, a novel and useful approach for hydrodynamical simulations is to calibrate the feedback efficiency to reproduce the present-day GSMF. This is the approach adopted by the EAGLE simulation (Schaye et al. 2015; Crain et al. 2015).

Is a simulation that reproduces the GSMF, and thus presumably also the stellar to halo mass relation, also able to reproduce the galaxy-galaxy signal as a function of galaxy stellar mass? This is not a trivial question to ask since, even if the correct stellar mass is assigned to haloes, there are other possible sources of discrepancy. In fact, the radial dependence of the galaxy-galaxy lensing signal depends also on the radial density profile of haloes, as well as the number and position of satellite galaxies within their host haloes. To answer this question, we compute predictions from the EAGLE hydrodynamical cosmological simulation of the galaxy-galaxy lensing profile at redshift zero. These predictions are compared with the observed signal measured using background galaxies imaged by the KiDS survey around spectroscopically confirmed foreground galaxies from the GAMA survey. KiDS (de Jong et al. 2013) is an optical imaging survey with the OmegaCAM wide-field imager (Kuijken 2011) on the VLT Survey Telescope (Capaccioli & Schipani 2011) with exquisite image quality. KiDS overlap with the Galaxy And Mass Assembly GAMA spectroscopic survey (Driver et al. 2011) which provides reliable redshift estimates and reliable group catalogues (for groups with more than four members with stellar masses above the completeness limit of GAMA). The combination of good image quality for shape determination of the source galaxies from KiDS and the spectroscopic redshift information of the lenses from GAMA provides an ideal set-up for galaxy-galaxy lensing measurements. In the rest of the paper we refer to the combination of KiDS and GAMA data with the term KiDSxGAMA. Recent works used the same observations to study the density profiles and masses of galaxy groups and clusters (Viola et al. 2015), as well as the total subhalo mass of satellite galaxies, the average satellite distance from the host halo and the average satellite-to-host mass ratio (Sifón et al. 2015).

This paper is organized as follows. In Section 5.2 we summarize important aspects of KiDSxGAMA, as well as a summary of the ESD measurements from galaxy shapes(§ 5.2.1). In § 5.2.2 we summarize the properties of the simulations employed in this study, the algorithm used to produce the group catalogue from simulations (§ 5.2.2) and the steps taken to measure the galaxy-galaxy lensing signal (§ 5.2.2). In Section 5.3 we report the results for the galaxy-galaxy lensing signal from simulations and the comparison with KiDSxGAMA data for central (§ 5.3.1) and satellites galaxies (§ 5.3.2). In § 5.3.3 we compare the $\Delta\Sigma$ profile for the whole galaxy population against the KiDSxGAMA observations as well as testing the effect of the stellar mass uncertainties on the simulation-observations comparison (§ 5.3.3). We discuss the limitations and the possible future improvements of this study in Section 5.4, we then summarize our findings and conclude in Section 5.5. In Appendix 5.A we test our results against changes in the simulation volume and resolution.

5.2 Methods

5.2.1 KiDSxGAMA

The data used in this paper are obtained from a cross-analysis of two surveys: KiDS and GAMA. KiDS is an ongoing ESO optical imaging survey (de Jong et al. 2013) with the OmegaCAM wide-field imager on the VLT Survey Telescope. When completed, it will cover a total area of 1500 square degrees in four bands (u, g, r, i). KiDS was designed to have both good galaxy shape measurements and photometric redshift estimates to identify the location of background galaxies. The mean redshift of the sources is $z = 0.55$.

In this paper, we use the initial galaxy-galaxy lensing measurements based on observations from KiDS covering 100 square degrees in all four optical bands. Their data are part of the first and second 'KiDS-DR1/2' data releases to the ESO community, as described in de Jong et al. (2015).

A key feature of the KiDS survey is the overlap with the GAMA spectroscopic survey (Driver et al. 2011) carried out using the AAOmega multi-object spectrograph on the Anglo-Australian Telescope (AAT). The GAMA survey is 98% complete down to r-band magnitude 19.8, and covers $\sim$ 180 square degrees of sky. The available spectroscopy allows reliable identification of galaxy groups (Robotham et al. 2011), which in turn permits a separation between central and satellite galaxies. This distinction will be used extensively throughout the paper. The redshift distribution of GAMA galaxies (median redshift $z \sim 0.25$) is ideal for measurements of the galaxy-galaxy lensing signal.

GAMA group finder

One of the main products of the GAMA survey is the group catalogue, G3Cv7 (Robotham et al. 2011). The group finder is based on a friends-of-friends (FoF) algorithm, which links galaxies based on their projected and line-of-sight proximity. Groups are therefore identified using spatial and spectroscopic redshift information (Baldry et al. 2014) of all the galaxies targeted by GAMA. The linking length has been calibrated using mock data (Robotham et al. 2011; Merson et al. 2013) from the Millennium simulation (Springel et al. 2005). The calibration also ensures that the grouping algorithm reproduces the basic properties, such as the mass, radius and velocity dispersion of FoF groups found in simulations with linking length of $b = 0.2$ and has thus been used as a base for the mock catalogue. The group catalogue has been tested against the mock data and ensures reliable central-satellite distinction against interlopers for groups with 5 or more members, $N_{\rm FoF} \geq 5$, above the completeness limit of GAMA of approximately $\log_{10}(M_{\rm star}[\,{\rm M}_{\odot}]) = 8$ (Robotham et al. 2011). Throughout the paper, unless stated otherwise, the galaxy-galaxy lensing signal is only computed for galaxies in groups with 5 or more members, $N_{\rm FoF} \geq 5$. This selection leaves 18712 out of an initial sample of 58642 galaxies in the overlapping region with the KiDS DR1 and DR2.

Lensing analysis

The galaxy-galaxy lensing measurements are based on the r-band exposures since these yield the highest image quality in KiDS. The images are then processed with the THELI pipeline (optimized for lensing applications, Erben et al. 2013), and galaxy ellipticities are derived using the LENSFIT code (Miller et al. 2007; Kitching et al. 2008; Miller et al. 2013).

The LENSFIT algorithm gives an estimate of the ellipticity (e_1, e_2) with respect to an equatorial coordinate system for every galaxy. Shape measurements are calibrated against a multiplicative bias that arises from the non-linear transformation of the image pixels for galaxies with low signal-to-noise ratio and small sizes (e.g., Melchior & Viola 2012; Refregier et al. 2012; Miller et al. 2013; Viola et al. 2014) using the same method as in Miller et al. (2013). The biases from non-perfect PSF deconvolution, centroid bias and pixel level detector effects are quantified and corrected for using the residual average ellipticity over the survey area. More details can be found in Kuijken et al. (2015) .

For every source-lens pair the measured ellipticity of the source is projected along the separation of the lens in a tangential (e_+) and cross ($e_\times$) component as:

$$\begin{pmatrix} e_+ \\ e_\times \end{pmatrix} = \begin{pmatrix} -\cos(2\Phi) & -\sin(2\Phi) \\ \sin(2\Phi) & -\cos(2\Phi) \end{pmatrix} \begin{pmatrix} e_1 \\ e_2 \end{pmatrix}, \tag{5.1}$$

where Φ is the position angle of the source with respect to the lens. Each lens-source pair is then assigned a weight

$$\tilde{w}_{\rm ls} = w_{\rm s}\tilde{\Sigma}_{\rm crit}^{-2}, \tag{5.2}$$

which is the product of the LENSFIT weight $w_{\rm s}$, assigned according to the estimated reliability of the source ellipticity (Miller et al. 2007), and $\tilde{\Sigma}_{\rm crit}$ which assigns a weight that is proportional to the lens-source pair distance, effectively down-weighting pairs that are close together and so less sensitive to lensing. The effective critical surface density, $\tilde{\Sigma}_{\rm crit}$, is:

$$\tilde{\Sigma}_{\rm crit} = \frac{4\pi G}{c^2} \int_{z_{\rm l}}^{\infty} \frac{D_{\rm l}(z_{\rm l}) D_{\rm ls}(z_{\rm l} z_{\rm s})}{D_s(z_{\rm s})} p(z_{\rm s}) {\rm d}z_{\rm s}, \tag{5.3}$$

where $D_{\rm l}$ is the angular diameter distance of the lens calculated using the spectroscopic redshift $z_{\rm l}$, D_s is the angular diameter distance of the source, $p(z_{\rm s})$ is the redshift distribution of the sources, and $D_{\rm ls}$ is the distance between the lens and the source. The distances of the lenses are known from the GAMA spectroscopy whereas for the sources the distances are computed based on the photometric redshifts derived from the KiDS-ESO-DR1/2 *ugri* images in the ESO data release. The the excess surface density, ESD, is then computed in bins of projected distance $r_{\rm p}$:

$$\Delta\Sigma(r_{\rm p}) = \gamma_{\rm t}(r_{\rm p})\tilde{\Sigma}_{\rm crit} = \left(\frac{\sum_{\rm ls} \tilde{w}_{\rm ls} e_+ \tilde{\Sigma}_{\rm crit}}{\sum_{\rm ls} \tilde{w}_{\rm ls}} \right) \frac{1}{1 + K(r_{\rm p})} \tag{5.4}$$

where the sum is over all source-lens pairs in the distance bin, and

$$K(r_{\rm p}) = \frac{\sum_{\rm ls} \tilde{w}_{\rm ls} m_{\rm s}}{\sum_{\rm ls} \tilde{w}_{\rm ls}} \tag{5.5}$$

is the correction to the ESD profile that takes into account the multiplicative noise bias $m_{\rm s}$ in the LENSFIT shape estimates. Typically, the value of the $K(r_{\rm p})$ correction is around 0.1, largely independent of $r_{\rm p}$.

Galaxy-galaxy lensing offers a direct measure of the $\Delta\Sigma$ profile:

$$\gamma_{\rm t}(r_{\rm p})\tilde{\Sigma}_{\rm crit} = \Delta\Sigma(r_{\rm p}) \equiv \bar{\Sigma}(< r_{\rm p}) - \Sigma(r_{\rm p}), \tag{5.6}$$

where $\Delta\Sigma$ is the difference between the surface density averaged within, and measured at, $r_{\rm p}$ ($\bar{\Sigma}(< r_{\rm p})$ and $\Sigma(r_{\rm p})$, respectively). This implies that the $\Delta\Sigma$ calculated from simulations using mass surface densities can be directly compared to the observed $\Delta\Sigma$ from weak lensing analysis.

The error on the ESD measurement is then estimated by:

$$\sigma^2_{\Delta\Sigma} = \sigma^2_{e_+} \left(\frac{\sum_{\rm ls} \tilde{w}^2_{\rm ls} \tilde{\Sigma}^2_{cr}}{(\sum_{\rm ls} \tilde{w}_{\rm ls})^2} \right), \tag{5.7}$$

where $\sigma^2_{e_+}$ is the variance of all source ellipticities combined. The ESD calculated from Eq. 5.4 can be directly compared to the ESD signal calculated from the simulations (see Eq. 5.6).

5.2.2 Simulations

We compare the observations to the hydrodynamical cosmological simulations from the EAGLE project (Schaye et al. 2015; Crain et al. 2015) with a cubic volume of 100 Mpc per side. EAGLE was run using a modified version of the *N*-Body Tree-PM smoothed particle hydrodynamics (SPH) code GADGET-3, which was last described in Springel (2005). The main modifications with respect to GADGET-3 regard the formulation of the hydrodynamics, the time stepping and the subgrid physics. Dark matter and baryons are represented by 2×1504^3 particles, with an initial particle mass of $m_{\rm b} = 1.2 \times 10^6\, h^{-1}\,{\rm M}_\odot$ and $m_{\rm dm} = 6.6 \times 10^6\, h^{-1}\,{\rm M}_\odot$ for baryons and a dark matter, respectively. EAGLE was run using the set of cosmological values suggested by the Planck mission $\{\Omega_{\rm m},\ \Omega_{\rm b}, \sigma_8,\ n_{\rm s},\ h\} = \{0.307, 0.04825, 0.8288, 0.9611, 0.6777\}$ (Table 9; Planck Collaboration et al. 2013).

EAGLE includes element-by-element radiative cooling (for 11 elements; Wiersma et al. 2009a), pressure and metallicity-dependent star formation (Schaye 2004; Schaye & Dalla Vecchia 2008), stellar mass loss (Wiersma et al. 2009b), thermal energy feedback from star formation (Dalla Vecchia & Schaye 2012), angular momentum dependent gas accretion onto supermassive black holes (Rosas-Guevara et al. 2013) and AGN feedback (Booth & Schaye 2009; Schaye et al. 2015). The subgrid feedback parameters were calibrated to reproduce the present day observed GSMF as well as the sizes of galaxies (Schaye et al. 2015). More information regarding the technical implementation of hydro-dynamical aspects as well as subgrid physics can be found in Schaye et al. (2015).

Halo catalogue

Groups of connected particles are identified by applying the FoF algorithm (Davis et al. 1985) to the dark matter particles using a linking length of 0.2 times the mean interparticle separation. Baryons are then linked to their closest dark matter particle and they are assigned to the same FoF group, if any. Subhaloes in the FoF group are identified using SUBFIND (Springel et al. 2001; Dolag et al. 2009). SUBFIND identifies local minima in the gravitational potential using saddle points. All particles that are gravitationally bound to a local minimum are grouped into a subhalo. Particles that are bound to a subhalo belong to that subhalo only. We define the subhalo center as the position of the particle for which the gravitational potential is minimum. The mass of a subhalo is the sum of the masses of all the particles that belong to that subhalo. The most massive subhalo is the *central* subhalo of a given FoF group and all other subhaloes are *satellites*.

The mass $M_{200}^{\rm crit}$ and the radius $r_{200}^{\rm crit}$ of the halo are assigned using a spherical over-density algorithm centered on the minimum of the gravitational potential, such that $r_{200}^{\rm crit}$ encompasses a region within which the mean density is 200 times the critical density of the universe.

An important aspect for the analysis is that the group finder of EAGLE links particles in real space whereas the GAMA group finder connects members in redshift space. This difference could be particularly important if a large fraction of interlopers were wrongly assigned to groups for GAMA. However, the GAMA group finder was tested against mock catalogues and found to be robust against interlopers for groups with 5 or more members ($N_{\rm FOF}^{\rm GAMA} \geq 5$) above the completeness limit of GAMA of approximately $\log_{10}(M_{\rm star}[\,{\rm M}_\odot]) = 8$ (Robotham et al. 2011).

Another caveat is that the galaxy sample in EAGLE can be considered to be volume limited whereas the galaxies in GAMA represent a flux limited sample. This can produce differences for the selection of rich groups between simulations and observations, the impact of which will be studied in future work.

Computation of the galaxy-galaxy lensing signal in EAGLE

In section § 5.2.1 we showed that the galaxy-galaxy lensing signal from observations is a direct proxy for the $\Delta\Sigma$ profile. Therefore, in order to compare with the observations, we need to calculate the $\Delta\Sigma$ profiles from EAGLE.

To calculate the surface density of a subhalo, we project onto the $x - y$ plane all the particles within a sphere with radius $2\,h^{-1}$ Mpc centered on the location of the subhalo. We divide the projected radial range into 150 equally spaced bins. At every projected radius $r_{\rm p}$, we calculate the surface density within $r_{\rm p}$, $\bar{\Sigma}(< r_{\rm p})$, as the sum of the mass of all the particles within the projected radius $r_{\rm p}$, $M(< r_{\rm p})$, divided by the area $A = \pi r_{\rm p}^2$. The surface density at $r_{\rm p}$, $\Sigma(r_{\rm p})$, is the mass enclosed in the annulus with inner radius $(r_{\rm p} - \delta r_{\rm p}/2)$ and outer radius $(r_{\rm p} + \delta r_{\rm p}/2)$ divided by the area $2\pi r_{\rm p}\delta r_{\rm p}$, where $\log_{10}\delta r_{\rm p} = \log_{10}(2[\,h^{-1}\,{\rm Mpc}])/150$. We tested different choices for the shape and extension of the projection volume. In principle the lensing signal is affected by the matter between the source and the lens and not only up to a given radial distance. We verified that projecting a cylindrical section around the center of a subhalo instead of a sphere has a small effect on the ESD profile but a large impact on the computation time. We thus opted for the spherical region. We also tested the impact of a using different radii. Specifically, we found that using spheres of $3\,h^{-1}$ Mpc instead of $2\,h^{-1}$ Mpc has a negligible effect on the signal.

Subhaloes are binned according to their stellar mass, calculated as the sum over all stellar particles that belong to the subhalo. The $\Delta\Sigma$ in a given stellar mass bin is then calculated by averaging the $\Delta\Sigma$ profiles of single subhaloes. The statistical errors are calculated using bootstrapping: galaxies in each mass bin are re-sampled 1000 times and the standard deviation of the resulting distribution of mean values of $\Delta\Sigma$ is reported as a proxy for the 1-sigma error.

5.3 Results

In the following we present the results for the excess surface density $\Delta\Sigma$ computed from the simulations (for details see §5.2.2). Galaxies are divided into 6 stellar mass bins ranging from $\log_{10}(M_{\rm star}[\,{\rm M}_\odot]) = 10$ to $\log_{10}(M_{\rm star}[\,{\rm M}_\odot]) = 11.8$. In the simulations we consider all stellar mass particles bound to a subhalo for the stellar mass determination. We note however that this choice may overestimate the stellar mass content of a galaxy since in observations stars in the galaxy outskirts are often not detectable. We address this caveat in § 5.3.3. The ESD in a given stellar mass bin is the mean value of the $\Delta\Sigma$ of all galaxies in that mass bin. The galaxy center is defined by the position of the particle belonging to the subhalo hosting the galaxy, for which the gravitational potential is minimal. The $\Delta\Sigma$ profile is computed in the simulations using 150 equally spaced logarithmic radial bins up to $2\,h^{-1}$ Mpc.

We compare each prediction from the simulation to the corresponding data from KiD-SxGAMA. We note that we compare results from the EAGLE simulation at $z = 0$ with the ESD of galaxies that have a mean redshift of $z \approx 0.25$. This is expected to have a minor impact on our results, as discussed in Section 5.4. To ensure a fair and robust comparison between predictions and observations (see discussion in § 5.2.2), throughout the paper we consider only galaxies hosted by haloes with 5 or more members with stellar masses above $\log_{10}(M_{\rm star}[\,{\rm M}_\odot]) = 8$ unless otherwise specified (see § 5.3.3).

We first present results for central and satellite galaxies separately (see § 5.3.1 and § 5.3.2) and their comparison with observations (see § 5.3.1 and § 5.3.2). We then present the results for both galaxy types combined (§ 5.3.3). This signal can be interpreted as a linear combination of the signal from satellite and central galaxies, where the relative importance of either of the two terms is modulated by the value of the satellite fraction (§ 5.3.3).

$M_{\rm star}$ *	$M_{200}^{\rm crit}\vert_{\rm cen}$ **	$M_{200}^{\rm crit}\vert_{\rm sat}$ **	$M_{\rm sub}^{\rm cen}$ **	$M_{\rm sub}^{\rm sat}$ **	$M_{\rm sub}^{\rm sat}/M_{200}^{\rm crit}$	$d_{\rm sat}$ ***	$r_{\rm half}^{\rm dm}\vert_{\rm cen}$ ***	$r_{\rm half}^{\rm dm}\vert_{\rm sat}$ ***	$N_{\rm gal}$	$f_{\rm sat}^{\rm EAGLE}$	$f_{\rm sat}^{\rm GAMA}$
(1)	(2)	(3)	(4)	(5)	(6)	(7)	(8)	(9)	(10)	(11)	(12)
[10.0 – 10.3]	11.96	13.80	12.01	11.18	0.04	575.9	90.2	17.0	586	0.96	0.99
[10.3 – 10.6]	12.17	13.83	12.19	11.46	0.06	608.7	100.4	22.3	498	0.85	0.97
[10.6 – 10.9]	12.42	13.87	12.46	11.80	0.07	806.5	113.0	30.6	375	0.57	0.93
[10.9 – 11.2]	12.71	13.98	12.75	12.23	0.09	805.3	139.7	47.8	241	0.28	0.78
[11.2 – 11.5]	13.11	14.03	13.13	12.48	0.06	624.7	186.4	51.6	106	0.10	0.46
[11.5 – 11.8]	13.51	14.17	13.53	12.81	0.07	615.1	257.0	67.8	32	0.16	0.22

Table 5.1: Values at $z = 0$ of various quantities of interest for each stellar mass bin. From left to right of the columns list: (1) stellar mass range; (2) average value of the host halo mass, $M_{200}^{\rm crit}$, for central galaxies; (3) same as (2) but for satellite galaxies; (4) mean value of the subhalo mass for central galaxies, considering all the particles bound to the subhalo; (5) same as (4) but for satellite galaxies; (6) average ratio between the mass of the satellite subhalo, $M_{\rm sub}$, and the mass of its host halo $M_{200}^{\rm crit}$; (7) average 3D distance between the satellite galaxy and the center of its host halo; (8) mean radius of central galaxies within which half of the mass in dark matter is enclosed; (9) same as (8) but for satellite galaxies; (10) total number of galaxies in the stellar mass bin; (11) average satellite fraction expressed as the total number of satellites divided by the total number of galaxies in the mass bin; (12) average satellite fraction in GAMA.

* $\log_{10}(M/[\,{\rm M}_\odot])$
** $\log_{10}(M/[\,h^{-1}\,{\rm M}_\odot])$
*** $R/[\,h^{-1}\,{\rm kpc}]$

5.3.1 The galaxy-galaxy lensing signal around central galaxies

The left panel of Fig. 5.1 shows the ESD profile around central galaxies in the EAGLE simulation as a function of the projected distance from the center of the galaxy. In all mass bins $\Delta\Sigma$ is a monotonically decreasing function of the projected radius. This is expected since the matter density peaks at the center of the halo where the central galaxy resides. Fluctuations in the surface density profiles can arise due to the presence of satellites, but these are usually not massive enough to significantly alter the azimuthally averaged surface density. Moreover, since the signal is averaged over many galaxies, any deviation due to a single massive satellite would be averaged out in the stacking process.

The right panel of Fig. 5.1 shows the values of $\Delta\Sigma$ at a separation $r_{\rm p} = 0.05\,h^{-1}\,{\rm Mpc}$ (red curve) as a function of stellar mass, normalized to the value in the stellar mass bin $10 < \log_{10}(M_{\rm star}[\,{\rm M}_{\odot}]) < 10.3$. We also report the mean $M_{\rm sub}$ as a function of stellar mass (black curve), normalized to the subhalo mass of galaxies in $10 < \log_{10}(M_{\rm star}[\,{\rm M}_{\odot}]) < 10.3$. Both $\Delta\Sigma(r_{\rm p} = 0.05\,h^{-1}\,{\rm Mpc})$ and the the mean mass $M_{\rm sub}$ are monotonically increasing functions of the stellar mass. The slopes of the two relations are different: $\Delta\Sigma(r_{\rm p} = 0.05\,h^{-1}\,{\rm Mpc})$ shows a weaker dependence on stellar mass (with a slope of 0.6), whereas $M_{\rm sub}$ increases linearly with the stellar mass. This is in line with the fact that haloes do not have single power law matter density profiles but a double power law with the characteristic radius depending on halo mass. Nonetheless, central galaxies with higher $\Delta\Sigma$ amplitudes are hosted by more massive haloes. Therefore, the amplitude of the $\Delta\Sigma$ profile at small scales is a proxy for the typical mass of the subhaloes hosting central galaxies in a given stellar mass bin.

Comparison with observations

Fig. 5.2 shows the $\Delta\Sigma$ signal in EAGLE (red curves) whereas $\Delta\Sigma$ from the observations is indicated with black diamonds. For stellar masses $10 < \log_{10}(M_{\rm star}[\,{\rm M}_{\odot}]) < 10.9$ the uncertainties in the data are large due to the limited number of low mass galaxies that are centrals in rich groups ($N_{\rm FoF} \geq 5$) and therefore not representative of the entire central galaxy population (Viola et al. 2015). For stellar masses $10.6 < \log_{10}(M_{\rm star}[\,{\rm M}_{\odot}]) < 11.5$ the uncertainties are smaller and the radial dependence of the signal is better constrained.

For the three most massive stellar mass bins the normalization and the radial dependence of the signal from EAGLE are consistent with the KiDSxGAMA data. For $11.2 < \log_{10}(M_{\rm star}[\,{\rm M}_{\odot}]) < 11.5$ the observed $\Delta\Sigma$ seems to favour a shallower excess surface density profile at radii larger than $400\,h^{-1}$ kpc. Note, however, that the error bars in EAGLE are asymmetric and correlated; consequently the estimates of $\Delta\Sigma$ appear more significant than they are.

The agreement between the ESD in EAGLE and KiDS suggest that central galaxies, with masses $10.9 < \log_{10}(M_{\rm star}[\,{\rm M}_{\odot}]) < 11.8$, are hosted in the simulation by subhaloes of approximately the correct mass and the right density profile. This is perhaps not surprising considering that EAGLE was calibrated to reproduce the GSMF and therefore to assign the correct stellar mass to subhaloes. The typical host halo masses predicted by EAGLE for galaxies in the 6 stellar mass bins shown can be found in Table 5.1, column (3). We have computed analytical $\Delta\Sigma$ profiles corresponding to haloes with NFW matter density profiles for the halo masses reported in Table 5.1. These analytical profiles reproduce the overall normalisation of the signal but poorly match the radial dependence of the numerical profiles. At this stage we speculate that this might be due to having assumed an incorrect concentration-halo mass relation and/or having neglected the contribution of baryonic matter to the $\Delta\Sigma$ profile. We defer a systematic analysis of this mismatch to future investigations.

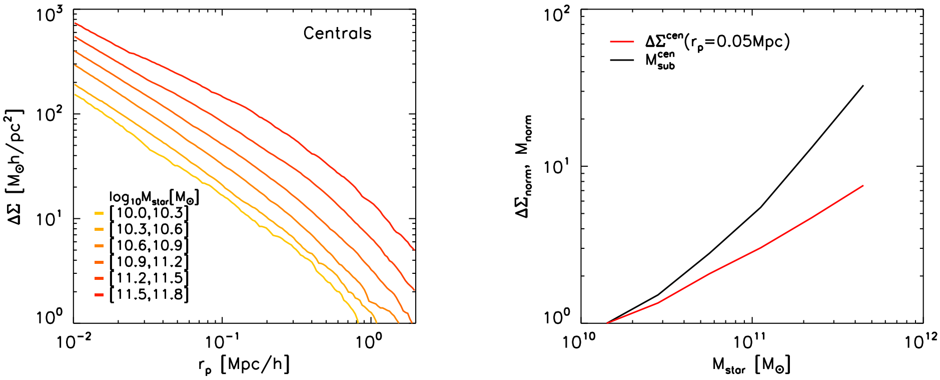

Figure 5.1: *Left panel*: Profiles of the excess surface density, $\Delta\Sigma$, of matter around central galaxies up to projected separations of $2\,h^{-1}$ Mpc from the center of the galaxy. Only galaxies hosted by groups with 5 or more members with stellar mass $\log_{10}(M_{\rm star}[\,{\rm M}_\odot]) > 8$ are taken into account for this analysis in order to mimic the GAMA selection of galaxies. Central galaxies are divided into 6 stellar mass bins ranging from $\log_{10}(M_{\rm star}[\,{\rm M}_\odot]) = 10$ to $\log_{10}(M_{\rm star}[\,{\rm M}_\odot]) = 11.8$. *Right panel*: The values of $\Delta\Sigma$ at a separation $r_{\rm p} = 0.05\,h^{-1}$ Mpc as a function of stellar mass (red curve), normalized by the value in the stellar mass bin $10 < \log_{10}(M_{\rm star}[\,{\rm M}_\odot]) < 10.3$. The mean $M_{\rm sub}$ as a function of stellar mass (black curve), normalized by the subhalo mass value for galaxies in $10 < \log_{10}(M_{\rm star}[\,{\rm M}_\odot]) < 10.3$, is also reported. The slope of the linear function fitting the $\Delta\Sigma$ values at the separation $r_{\rm p} = 0.05\,h^{-1}$ Mpc is 0.59 whereas for $M_{\rm sub}$ the slope is 1.01.

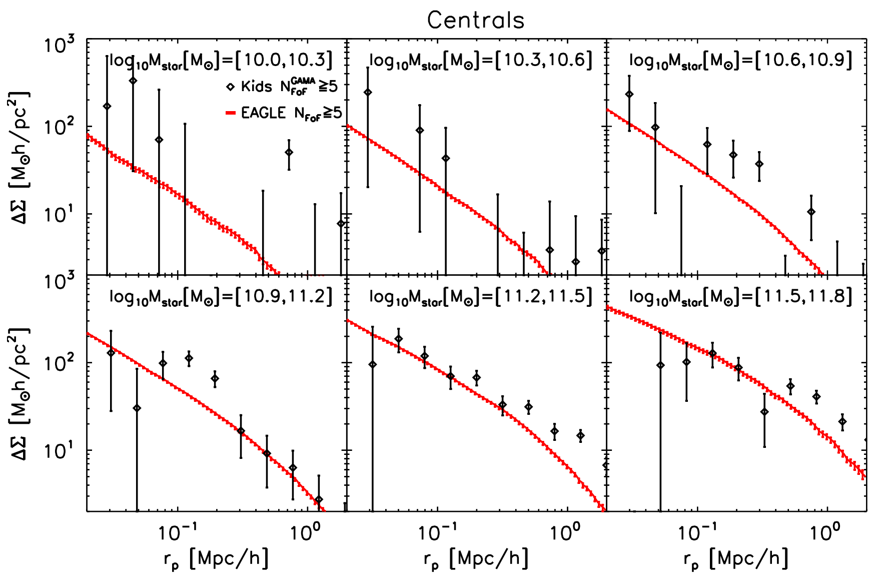

Figure 5.2: Excess surface density profiles in the KiDS survey (black diamonds) and in the EAGLE simulation (red curves) for central galaxies hosted by groups with 5 or more members that each have stellar masses greater than $\log_{10}(M_{\rm star}[\,{\rm M}_\odot]) = 8$ in order to mimic the GAMA selection of galaxies. Each panel contains a different bin in central galaxy stellar mass. Asymmetric error bars show the 1-σ scatter in each $r_{\rm p}$ bin.

5.3.2 The galaxy-galaxy lensing signal around satellite galaxies

Unlike central galaxies, the $\Delta\Sigma$ profiles of the satellites galaxies are *not* expected to be monotonically decreasing functions of the separation from the centre. For a single satellite galaxy the profile should become negative at the projected separation from the center of the host halo (Yang et al. 2006). This effect is due to the surface density at the center of the host halo being larger than the mean internal surface density, $\Sigma(r^{\rm halo}_{\rm p,center}) > \bar{\Sigma}(< r^{\rm halo}_{\rm p,center})$. At larger separations than the distance to the host halo, the $\Delta\Sigma$ profile first increases due to the inclusion of the center of the host halo in the term $\Sigma(< r_{\rm p})$, before decreasing again at still larger separations. Stacking the $\Delta\Sigma$ of satellites in a given stellar mass bin averages out the negative parts of the profiles since the distances between each satellite and its host halo are different. On the other hand, the increase in the signal at larger radii is preserved by the stacking; the amplitude of the satellite bump can be used as a proxy for the typical mass of the host haloes in which satellites reside.

The left panel of Fig. 5.3 shows the excess surface density as a function of the projected distance from the center of the satellite galaxy. The small scale ($r_{\rm p} = 0.05\,h^{-1}$ Mpc) normalization of the $\Delta\Sigma$ profile is an increasing function of the stellar mass of the satellite. The three lowest stellar mass bins show a comparable amplitude of the satellite bump. This similarity can be explained by the fact that the richness cut effectively selects host haloes by mass. In fact, most of the satellites with stellar mass $10 < \log_{10}(M_{\rm star}[\,{\rm M}_\odot]) < 10.9$ reside in host haloes of comparable masses ($\log_{10}(M^{\rm crit}_{200}[\,h^{-1}\,{\rm M}_\odot]) \approx 13.8$; see also Table 5.1, column (3)). The prominence of the satellite bump decreases up to $\log_{10}(M_{\rm star}[\,{\rm M}_\odot]) = 11.2$, a trend that is explained by the fact that the ratio $M^{\rm sat}_{\rm sub}/M^{\rm crit}_{200}$ increases from 0.04 to 0.09 in the considered mass range (see Table 5.1, column 6). For higher stellar mass bins, the relative importance of the satellite bump decreases.

The radius at which the excess surface density profile starts to be dominated by the host halo mass (the satellite bump) increases with stellar mass up to $\log_{10}(M_{\rm star}[\,{\rm M}_\odot]) = 11.2$. This effect is driven by the increasing average distance between satellites and their host haloes raising from $\sim 500\,h^{-1}$ kpc to $\sim 800\,h^{-1}$ kpc in the mass range considered (see table 5.1, column (7)).

The right panel of Fig. 5.3 shows $\Delta\Sigma$ for satellite galaxies at a separation $r_{\rm p} = 0.05\,h^{-1}$ Mpc (blue continuous curve) and at separation $r_{\rm p} = 0.5\,h^{-1}$ Mpc (blue dashed curve), as a function of stellar mass, normalized by their values in the stellar mass bin $10 < \log_{10}(M_{\rm star}[\,{\rm M}_\odot]) < 10.3$. The mean $M_{\rm sub}$ (black continuous curve) and the host halo mass $M^{\rm crit}_{200}$ (black dashed curve) are also shown as a function of stellar mass.

At smaller separations ($r_{\rm p} = 0.05\,h^{-1}$ Mpc), the ESD of satellite galaxies increases with stellar mass. The same trend is shared by the average subhalo mass for satellite galaxies since satellites with higher stellar masses are hosted by more massive dark matter subhaloes. As in the case of central galaxies, the similar dependence on the stellar mass suggests that the amplitude of $\Delta\Sigma$ at small separations can be considered a proxy for the subhalo mass hosting the satellite galaxy.

For larger separations ($r_{\rm p} = 0.5\,h^{-1}$ Mpc), the $\Delta\Sigma$ profile starts to be dominated by the contribution of the halo hosting the satellite galaxy. In this case $\Delta\Sigma$ shares a similar trend with stellar mass as the mean host halo mass for satellite galaxies, $M^{\rm crit}_{200}$. The dependence on stellar mass is remarkably similar for both quantities and shows very little variation up to $\log_{10}(M_{\rm star}[\,{\rm M}_\odot]) = 10.9$ since, as discussed before, the richness cut effectively results in a selection in host halo mass as well. The similar dependence of $\Delta\Sigma$ with halo mass at larger radii highlights the fact that the amplitude of the satellite bump is tightly correlated to the host halo mass. In principle the amplitude of the satellite bump should depend on the satellite's subhalo mass as well as on the host halo mass. In practice the satellite's subhalo mass is

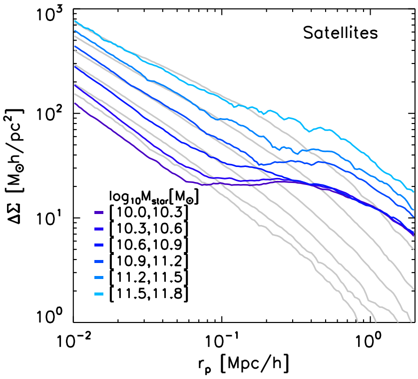

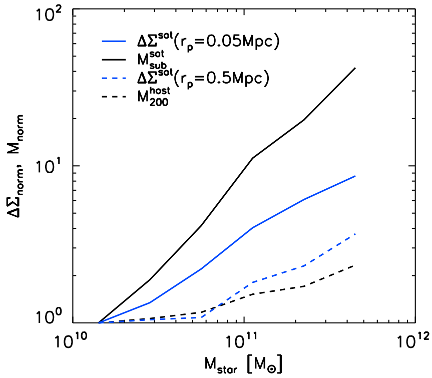

Figure 5.3: As in Fig. 5.1 but for satellite galaxies. To ease the comparison in the left panel, the results for the central galaxies are reported with gray curves. In the right panel the value of $\Delta\Sigma(r_p = 0.5\,h^{-1}$ Mpc) is reported as a function of the stellar mass (blue dashed curve) along with the mean host halo mass M_{200}^{crit} (black dashed curve). The slope of a linear fit of the $\Delta\Sigma$ values at a separation $r_p = 0.05\,h^{-1}$ Mpc is 0.65 whereas for M_{sub} the slope is 1.10.

always around $\sim 5\%$ of the host halo mass and therefore it plays a minor role in setting the amplitude of the satellite bump. We note that the ratio M_{sub}/M_{200}^{crit} is often inferred in N-body simulations or in semi-analytical models of infalling satellite galaxies (e.g. van den Bosch et al. 2005; Jiang & van den Bosch 2014) and it has been recently measured via galaxy-galaxy lensing by Sifón et al. (2015) who report values ranging from 0.005 to 0.015, in agreement with our results.

Comparison with observations

Fig. 5.4 shows the comparison between the observed $\Delta\Sigma$ profile of satellite galaxies in KiD-SxGAMA (black squares) and the corresponding signal in the EAGLE simulations (blue curves) for 6 stellar mass bins. For all stellar masses there is good agreement between simulation and observation in both the predicted normalization of the ESD profile and in the location and the amplitude of the satellite bump.

For stellar masses $10.6 < \log_{10}(M_{star}[\mathrm{M}_\odot]) < 10.9$ the data show a dip in the $\Delta\Sigma$ profile at $r_p \sim 100\,h^{-1}$ kpc that is not present in the simulations. This unreproduced feature can be due to a different radial distribution of satellite galaxies in the simulation and observations. For example, if a large part of the satellites in the observations are located in a very narrow range of distances from their host haloes this can produce a similar dip in the observed signal. On the other hand, it is quite unlikely that satellites of different host haloes are preferentially located at a particular distance from their hosts. The richness is likely to play a role since the dip is less pronounced in the signal computed using the full sample of galaxies without a richness cut (cf. Fig. 5.10). Understanding this feature in the observations would require a comparison of the radial distribution of satellites in both the simulation and observations. We leave this comparison to future work. The amplitude of the signal at small and large radii for this mass bin is well reproduced by the simulation.

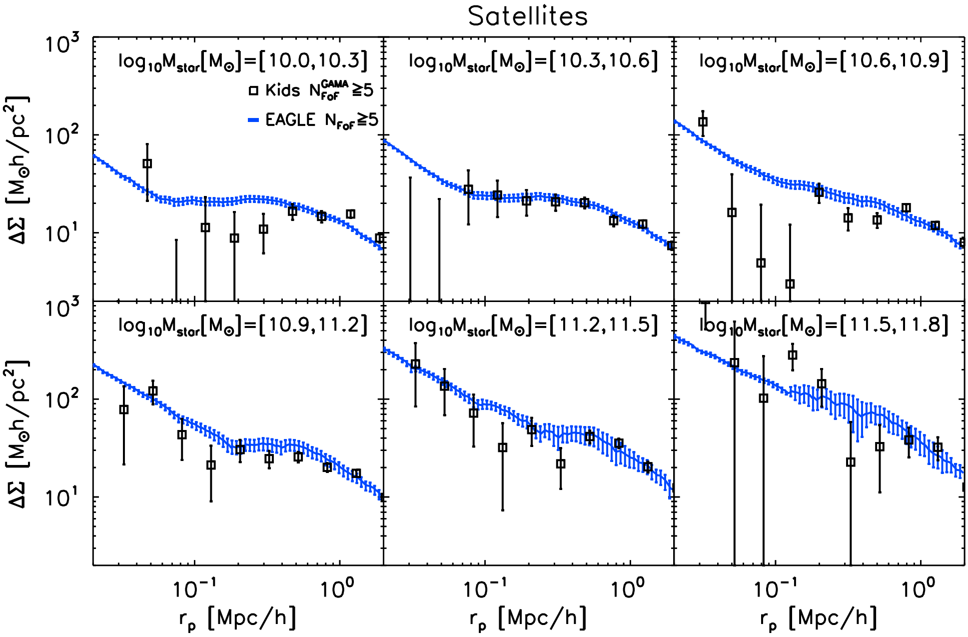

Figure 5.4: As in Fig. 5.2 but for satellite galaxies.

5.3.3 The galaxy-galaxy lensing signal around all galaxies

In this section we present the ESD calculated considering all galaxies without distinguishing between centrals and satellites, while still selecting only rich groups.

The $\Delta\Sigma$ profile of the whole population of galaxies of a given stellar mass is essentially the linear combination of the profiles for satellites, $\Delta\Sigma_{\rm sat}$, and centrals, $\Delta\Sigma_{\rm cen}$,:

$$\Delta\Sigma = f_{\rm sat}\Delta\Sigma_{\rm sat} + (1 - f_{\rm sat})\Delta\Sigma_{\rm cen} \tag{5.8}$$

where $f_{\rm sat}$ is the satellite fraction of galaxies in a given stellar mass bin. The relative importance of either of the two terms is set by the value of $f_{\rm sat}$.

In order to illustrate more clearly the role of the satellite fraction, in the left panel of Fig. 5.5 we show the ESD profile of galaxies in the stellar mass bin $10.9 < \log_{10}(M_{\rm star}[\,{\rm M}_{\odot}]) < 11.2$ for the central (red curve), the satellite (blue curve), and the full galaxy population (black curve).

The $\Delta\Sigma$ profiles for satellites and centrals have similar amplitudes at small radii, which implies that they have comparable central surface densities and subhalo masses. It is clear that the $\Delta\Sigma$ profile of the whole galaxy population lies in between those for satellite and central galaxies. In this mass bin $f_{\rm sat} \sim 28\%$; see Table 5.1 for the tabulated values in the other stellar mass bins.

The right panel of Fig. 5.5 shows the ESD as a function of the projected distance from the center of the galaxy for central and satellite galaxies combined. For stellar masses smaller than $\log_{10}(M_{\rm star}[\,{\rm M}_{\odot}]) = 10.9$ the signal is close to that of satellites (compare with Fig. 5.3). This is due to the high satellite fraction ($\geq 60\%$, see Table 5.1). For higher stellar mass bins the relative importance of the satellite component is downweighted by the lower satellite fractions. For $11.2 < \log_{10}(M_{\rm star}[\,{\rm M}_{\odot}]) < 11.8$ the satellite fraction is smaller than 20% and

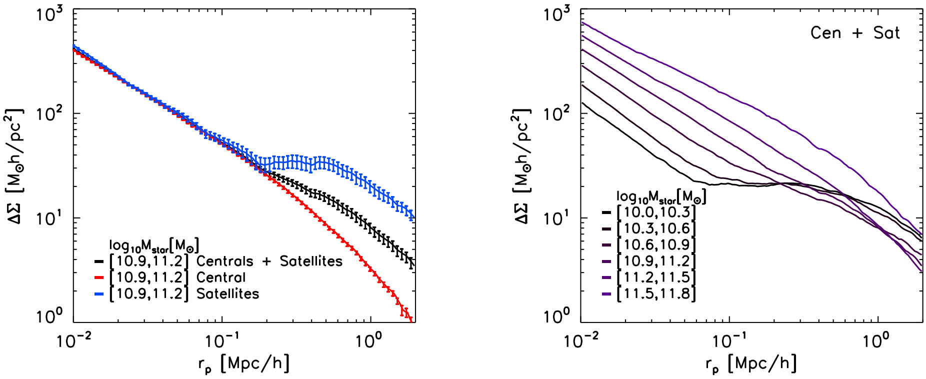

Figure 5.5: *Left panel*: Excess surface density for the central (red curves), the satellite (blue curve), and the full galaxy population (black curve) for a representative stellar mass bin ($10.9 < \log_{10}(M_{\rm star}[\,\mathrm{M}_\odot]) < 11.2$). Error bars show 1-$\sigma$ uncertainties calculated with a 1000 bootstrap resampling of the galaxies. *Right panel*: As in the left panel of Fig. 5.1 but for the full galaxy population (i.e. both centrals and satellites).

the total $\Delta\Sigma$ profile is almost completely dominated by the $\Delta\Sigma$ profile of the central galaxies (compare with Fig. 5.1).

Comparison with observations

In the previous section we underlined the importance of the satellite fraction in shaping the $\Delta\Sigma$ signal when both satellites and central galaxies are taken into account. It is of interest to start the comparison with the observational data by considering the satellite fraction in the simulation and in the observations. Fig. 5.6 shows the satellite fraction in EAGLE (black curve) and GAMA (blue filled circles) for groups with 5 or more members, as a function of stellar mass. We remind the reader that, as discussed in § 5.2.2 the group finders used in the simulation and observations are not identical, which could also lead to differences in the satellite-central galaxy classification. Moreover, since the GAMA survey is flux limited, some of the groups that are considered rich in EAGLE could have some of their satellites with stellar mass $\log_{10}(M_{\rm star}[\,\mathrm{M}_\odot]) < 8$, below the GAMA detection limit, thus excluded from the measurements. Due to this effect, groups in GAMA will tend to be systematically richer (especially at the high redshift end), resulting in a higher fraction of satellites with large stellar masses compared to the groups in EAGLE. Hence the satellite fraction at fixed stellar mass is expected to be higher for GAMA, which may potentially account for the discrepancies in the satellite fraction between the simulation and observations (at least partially). We defer a proper investigation of this effect to future work, as one would need to create mock GAMA observations from the EAGLE simulation.

The satellite fraction for stellar masses $\log_{10}(M_{\rm star}[\,\mathrm{M}_\odot]) < 10.9$ is close to one because rich groups are unlikely to have low-mass centrals. With increasing stellar mass the satellite fraction becomes smaller. There is a clear offset between the $f_{\rm sat}$ in simulations and observations. The satellite fraction in GAMA is consistently higher than in EAGLE and the difference is largest for $10.9 < \log_{10}(M_{\rm star}[\,\mathrm{M}_\odot]) < 11.2$. We also tested that the satellite fraction in EAGLE is well converged with resolution and simulation volume (not shown).

Fig. 5.7 compares the $\Delta\Sigma$ profiles obtained from observations using KiDSxGAMA (black

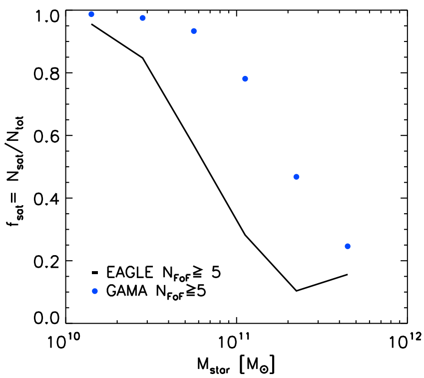

Figure 5.6: Satellite fraction, $f_{\rm sat}$, in EAGLE (black curve) and in KiDS (blue filled circles) for groups with 5 or more members with stellar mass above the stellar mass limit of $\log_{10}(M_{\rm star}[\,{\rm M}_\odot]) = 8$.

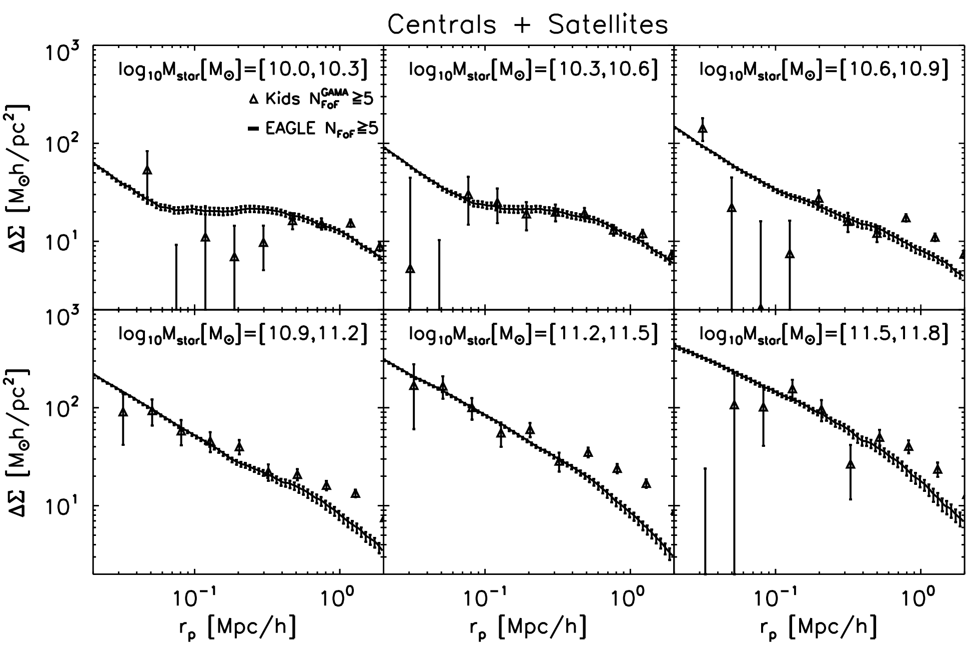

Figure 5.7: As in Fig. 5.2 but for the whole galaxy population (i.e. both centrals and satellites).

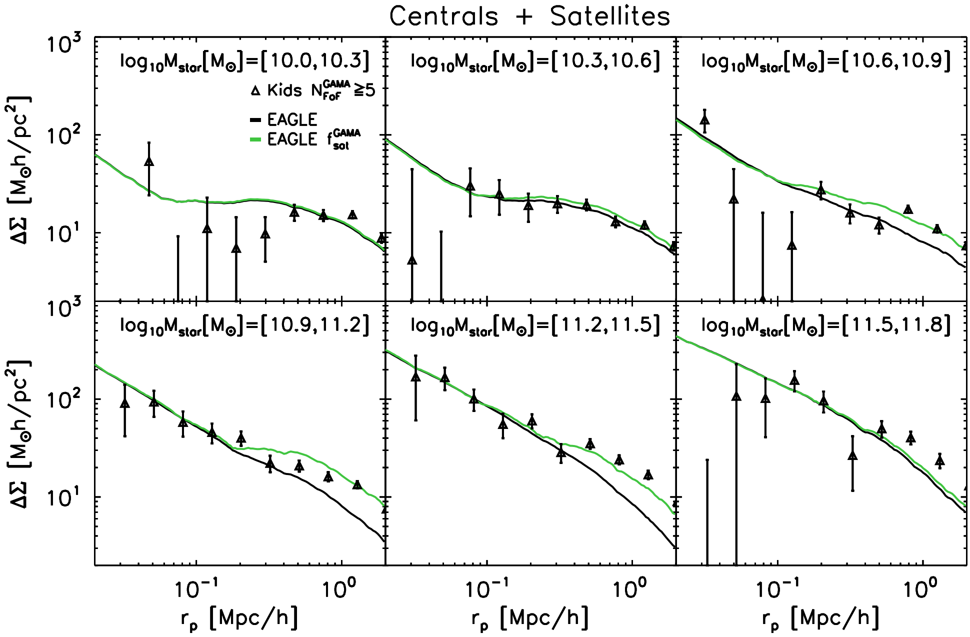

Figure 5.8: Excess surface density profiles in KidsxGAMA (data points), in EAGLE (black curves) and in EAGLE after rescaling by the satellite fraction from GAMA (green curves).

triangles) and the EAGLE simulations (black curves). Most of the differences between $\Delta\Sigma$ in the simulation and observations are in line with what we expect from our previous results. Specifically, the unreproduced dip at $r_{\rm p} \sim 100\,h^{-1}$ kpc for the mass bin $10.6 < \log_{10}(M_{\rm star}[\,{\rm M}_\odot]) < 10.9$ is a consequence of the same feature in the $\Delta\Sigma$ profile of satellites. In the same way, the steepness of the the outer profile for $10.9 < \log_{10}(M_{\rm star}[\,{\rm M}_\odot]) < 11.8$ arises from the different satellite fraction between EAGLE and GAMA, as $\Delta\Sigma$ for all galaxies is a linear combination of $\Delta\Sigma$ from satellite and central galaxies (see Eq. 5.8). A smaller satellite fraction tends to reduce $\Delta\Sigma$ at large separations (see left panel of Fig. 5.5). Therefore, since the satellite fraction in EAGLE is underestimated, $f_{\rm sat}$ might be responsible for the shallower $\Delta\Sigma$ profiles at large distances ($r_{\rm p} > 400$ kpc). In order to test this, we rescale $\Delta\Sigma$ from EAGLE by the observed satellite fraction:

$$\Delta\Sigma^{\rm EAGLE}_{\rm rescaled} = f^{\rm GAMA}_{\rm sat}\Delta\Sigma^{\rm EAGLE}_{\rm sat} + (1 - f^{\rm GAMA}_{\rm sat})\Delta\Sigma^{\rm EAGLE}_{\rm cen}, \tag{5.9}$$

where $f^{\rm GAMA}_{\rm sat}$ is the satellite fraction from GAMA.

Fig. 5.8 shows the rescaled $\Delta\Sigma$ profile for all galaxies (green curves) as well as the original EAGLE profile (black curves) and the observed signal from KiDS (black triangles). The rescaled signal better reproduces the shallow outer radial profile for the stellar mass bin $10.6 < \log_{10}(M_{\rm star}[\,{\rm M}_\odot]) < 11.5$. On the other hand, for $10.9 < \log_{10}(M_{\rm star}[\,{\rm M}_\odot]) < 11.2$ the amplitude of the satellite bump is now too high. As expected, the different satellite fractions have no influence on the $\Delta\Sigma$ profile at small radii ($r_{\rm p} < 100\,h^{-1}$ kpc).

The effect of stellar mass uncertainties in the comparison with observations

In the comparison between simulation and observations an important role is played by stellar mass errors, both random and systematic. We consider here the effect of a random error of ~ 0.1 dex (Behroozi et al. 2013) associated with uncertainties in the stellar mass estimation from broadband photometry. We are not considering here the effect of systematic errors that might arise from different choices in the stellar population synthesis model or in the initial stellar mass function. These errors can be significantly larger (~ 0.3 - 0.4 dex) (Conroy et al. 2009; Behroozi et al. 2010; Pforr et al. 2012; Mitchell et al. 2013) than the random error considered here.

In the case of random errors in the stellar mass estimation, since the number of galaxies decreases with stellar mass, there are always more low-mass galaxies scattered to high masses than vice versa (Furlong et al. 2015). The importance of this effect depends on the steepness of the GSMF. For low mass galaxies $\log_{10}(M_{\rm star}[\,{\rm M}_\odot]) < 10.9$ where the GSMF is reasonably flat, a comparable number of galaxies are scattered towards higher masses than to lower masses. On the other hand, for higher stellar masses where the GSMF is steeper, comparably more low mass galaxies are scattered towards higher masses. Therefore the effect of random errors is expected to be stronger at higher masses.

A potential source of systematic errors is the different definition of stellar mass in the simulation and observations. Throughout the paper we have defined the stellar mass of a galaxy as the sum of the masses of the stars bound to the subhalo hosting the galaxy. However, in observations stars that reside in the outskirts of a galaxy are often undetected and will thus not contribute to the stellar mass. We study this source of systematic errors by redefining stellar masses to include only stars in a given aperture (30 physical kpc, see the discussion in Schaye et al. (2015)). As for the previous case, this effect is expected to be stronger at higher masses, for which the typical extent of a galaxy is greater than 30 kpc.

Fig. 5.9 shows the $\Delta\Sigma$ profile for all galaxies in the case where a random error of 0.3 dex is applied to the stellar masses (purple dotted curves), as well as a case in which only stars within 30 kpc are considered for the computation of the stellar masses (orange dashed curves). For comparison we also show the original EAGLE profiles (black curves) and the observed signal from KiDS (black triangles).

The uncertainties in the stellar mass determinations play a very minor role for all stellar mass bins. The effect of random errors on the $\Delta\Sigma$ profiles is well within the errors on the simulation results (cf. Fig 5.7).

Including only stars within a 30 kpc aperture effectively lowers the stellar mass estimate of galaxies with $10.9 < \log_{10}(M_{\rm star}[\,{\rm M}_\odot]) < 11.8$. This systematic decrease of the stellar mass tends to assign galaxies, previously contributing to higher stellar mass bins, to lower stellar mass bins. Therefore, the average subhalo mass of galaxies in a given stellar mass bin is increased, which in turn increases the amplitude of the average $\Delta\Sigma$ profile in that bin.

We note that, due to the stochasticity of the stellar mass determination, when random errors are included different galaxies contribute to the $\Delta\Sigma$ profile in the different cases.

Comparison with observations without richness cut

So far we have only considered groups with 5 or more members with stellar mass above the stellar mass limit of $\log_{10}(M_{\rm star}[\,{\rm M}_\odot]) = 8$. Galaxies in rich groups are used to ensure a robust classification in central and satellite galaxies in GAMA for an easier interpretation of the signal of both populations combined. It is also of interest to compare the $\Delta\Sigma$ profile for all galaxies not selected by their host group richness.

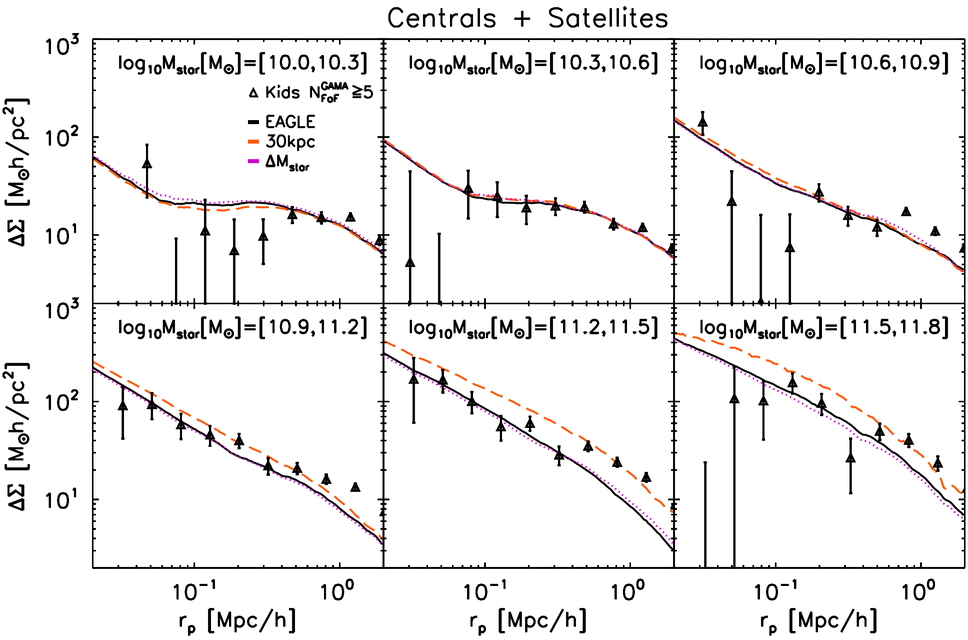

Figure 5.9: As in Fig. 5.7, but showing the $\Delta\Sigma$ profile for galaxies for which a random error in the stellar mass estimation of $\sim$ 0.1 dex is included (purple dotted curves), the $\Delta\Sigma$ profile of galaxies for which only stars within 30 kpc are considered (orange dashed curves), as well as the original EAGLE profile (black curves) and the observed signal from KiDS (black triangles).

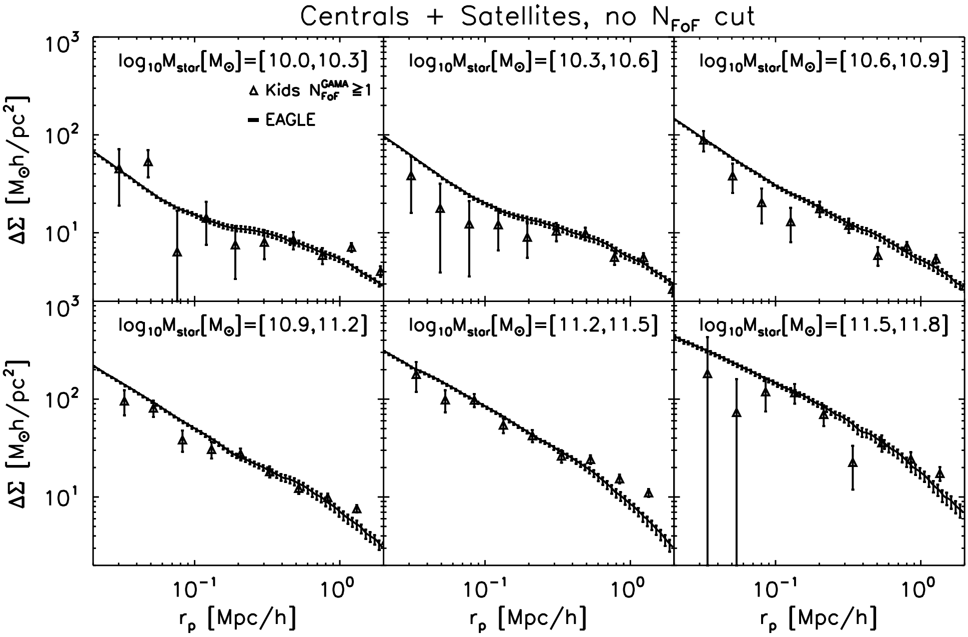

Figure 5.10: As in Fig. 5.7, but without a richness cut in both data and simulations.

Fig. 5.10 shows the $\Delta\Sigma$ profiles in EAGLE and in KiDSxGAMA for all galaxies irrespective of the richness of the group in which they reside. Due to the lower satellite fraction, at lower steller masses the amplitude of the satellite bump is reduced relative to that measured when including the richness cut (see Fig. 5.7). Without the richness cut the differences between EAGLE and the observations are smaller. However, for $10.3 < \log_{10}(M_{\rm star}[\,{\rm M}_\odot]) < 10.6$ the simulation slightly overestimates the $\Delta\Sigma$ profile, and therefore the masses of the haloes hosting these galaxies, which is consistent with the slight underestimate of the GSMF at these masses shown in Schaye et al. (2015). Also, for $10.6 < \log_{10}(M_{\rm star}[\,{\rm M}_\odot]) < 10.9$, the dip in the $\Delta\Sigma$ profile is less pronounced, suggesting that the richness cut could play a role in the strength of this feature.

5.4 Discussion

In this section we discuss some of the limitations of our study and we highlight possible future improvements. The main points are:

- The group finder of EAGLE identifies groups in real space whereas the GAMA group finder uses redshift space. This may cause differences in the $\Delta\Sigma$ profile, in particular if interlopers are wrongly assigned to groups, which would artificially increase the richness of the observed group. Therefore, the observed signal would be artificially lowered by the contribution of less massive groups hosting fewer than 5 members. To be fully consistent, the same algorithm should be employed in both simulations and observations.

- The GAMA survey is a flux limited survey whereas the EAGLE simulation can be considered as a volume limited one. In practice some of the groups that are considered rich in EAGLE could have some of their satellites with stellar mass $\log_{10}(M_{\rm star}[\,\mathrm{M}_\odot]) < 8$, below the GAMA detection limit, thus excluded from the measurements. Due to this effect, groups in GAMA with at least 5 detected members will tend to be systematically richer than EAGLE groups with 5 or more members with stellar mass $\log_{10}(M_{\rm star}[\,\mathrm{M}_\odot]) > 8$ (especially at the high redshift end), resulting in a higher fraction of satellites with large stellar masses compared to the groups in EAGLE. Hence the satellite fraction at fixed stellar mass is expected to be higher for GAMA, which may potentially account for the discrepancies in the satellite fraction between the simulation and observations (at least partially). Moreover, this effect could also explain why the agreement with EAGLE improves if no richness cut is applied to the data. We defer a proper investigation of this effect to future work, as one would need to create mock GAMA observations from the EAGLE simulation.

- The centering in observations is done according to the light emitted by the galaxies – the center of a group is defined as location of the Brightest Group Galaxy – whereas in simulations we adopt the minimum of the gravitational potential as the center. Thus any significant misalignment between the center of light and the deepest point in the gravitational potential could cause differences in our results. However Schaller et al. (2015), have shown that in EAGLE the majority of the galaxies ($> 95\%$) have offsets between the center of mass of their stellar and dark matter distribution that are smaller than the simulation's gravitational softening length (~ 700pc); Therefore, this effect is likely to be unimportant.

- The $\Delta\Sigma$ signal in KiDSxGAMA is calculated around galaxies that are on average at $z \sim 0.25$ whereas we compare the results from the EAGLE simulation at $z = 0$. This discrepancy is mitigated by the fact that from $z = 0.25$ to $z = 0$ there is little evolution in the GSMF (Furlong et al. 2015), but a consistent comparison should use the same redshift for the observations and the model.

- An interesting line of inquiry to better explain some of our results would be to compare the satellite radial distributions in the simulations and observations. This could potentially unveil the source of the unreproduced feature in the $\Delta\Sigma$ profile of satellite galaxies in $10.6 < \log_{10}(M_{\rm star}[\,\mathrm{M}_\odot]) < 10.9$.

- In this work we mostly assume that the good agreement between the simulation and observations stems from the ability of EAGLE to reproduce the observed GSMF. A comprehensive study should be made to test how sensitive this agreement is to the level at which the GSMF is reproduced by the simulations. This can be studied by employing the EAGLE models using different subgrid parameters (Crain et al. 2015).

5.5 Conclusions

In this work we compare the excess surface density signal $\Delta\Sigma$ obtained from the state-of-the-art hydrodynamical cosmological EAGLE simulation project to the observed weak galaxy-galaxy lensing signal using sources with accurate measurements from the KiDS survey around spectroscopically confirmed galaxies from GAMA.

We select galaxies in EAGLE that are hosted by groups with more than four members with stellar masses above the completeness limit of GAMA. For this selection the GAMA group catalogue has been tested to be robust against interlopers (Robotham et al. 2011).

Galaxies are divided into six logarithmically equispaced stellar mass bins in the range $10 < \log_{10}(M_{\rm star}[\,\mathrm{M}_\odot]) < 11.8$.

Thanks to the GAMA group catalogue the observed $\Delta\Sigma$ signal can be calculated independently for satellite and central galaxies. The $\Delta\Sigma$ signal from central galaxies (Fig. 5.1) in EAGLE is composed of a shallower inner part and a steeper outer part. We compare the $\Delta\Sigma$ signal from central galaxies in EAGLE with the observed signal in KiDS. For stellar mass bins for which the uncertainties on the data are small enough that the radial dependence on the signal can be appreciated ($10.6 < \log_{10}(M_{\rm star}[\,\mathrm{M}_\odot]) < 11.5$), the normalization and the radial dependence of the signal from EAGLE are consistent with the KiDSxGAMA data (Fig. 5.2). This suggests that the average subhalo mass, as well as the density profile of central galaxies in EAGLE, is consistent with observations.

The $\Delta\Sigma$ profiles of satellite galaxies show a deviation from the profiles of central galaxies due to the contribution to the surface density of the mass of the halo hosting the satellite galaxies (Fig. 5.3). Comparing the predicted satellite signal with observations, we find a good agreement with the exception of a notable feature in the $\Delta\Sigma$ profile of satellite galaxies for $10.6 < \log_{10}(M_{\rm star}[\,\mathrm{M}_\odot]) < 10.9$. The good agreement between data and simulation suggests that the density profile, the subhalo mass and the satellite-host mass ratio of satellite galaxies in EAGLE are consistent with observations.

The $\Delta\Sigma$ signal of the whole population of galaxies is a linear combination of the signals from satellite and central galaxies (left panel of Fig. 5.5) where the multiplicative factor is the fraction of galaxies, $f_{\rm sat}$, that are satellites. The slope of the signal depends on $f_{\rm sat}$, on their typical host halo mass and only minimally on the typical subhalo masses of satellites (right panel of Fig. 5.5). This result indicates that galaxy-galaxy lensing has the potential to constrain quantities, such as $f_{\rm sat}$, that are not strictly dependent on the stellar-halo mass relation.

The differences between observations and the simulation in the steepness of the outer $\Delta\Sigma$ profile (Fig. 5.7), for all galaxies with $10.9 < \log_{10}(M_{\rm star}[\,\mathrm{M}_\odot]) < 11.8$, originate from the different satellite fractions in EAGLE and GAMA (Fig. 5.6). Indeed, after rescaling the total signal in EAGLE by the observed satellite fraction from GAMA the agreement with the data improves (Fig. 5.8). The discrepancies in the satellite fraction potentially originate from the comparison of a flux-limited sample (GAMA) to a volume-limited one (EAGLE). This effect could explain, at least partially, the differences in the satellite fraction of EAGLE and GAMA.

Including only stars within an aperture of 30 kpc, to account for the caveat that only stars in the inner part of a galaxy are detected in observations, increases the ESD profile (see fig. 5.9) because in this procedure the same stellar masses are obtained for more massive haloes.

Without the richness cut the differences between EAGLE and the observations are somewhat smaller, although some discrepancies are still present (see Fig. 5.10).

We discussed some possible caveats of this study (see Section 5.4), such as the difference between the halo finders of EAGLE and GAMA and the use of $z = 0$ results from EAGLE to compare with $z = 0.25$ median redshift observations of the GAMA galaxies. We argue that these limitations are unlikely to affect our results significantly. We suggest some possible future improvements of this study such as the comparison of the radial distributions of satellites in EAGLE and GAMA as well as a study of the sensitivity of $\Delta\Sigma$ profiles on the level with which the GSMF is reproduced by the simulation.

Bibliography

Anderson, L., Aubourg, É., Bailey, S., et al. 2014, MNRAS, 441, 24

Baldry, I. K., Alpaslan, M., Bauer, A. E., et al. 2014, MNRAS, 441, 2440

Behroozi, P. S., Conroy, C., & Wechsler, R. H. 2010, ApJ, 717, 379

Behroozi, P. S., Wechsler, R. H., & Conroy, C. 2013, ApJ, 770, 57

Bolton, A. S., Burles, S., Koopmans, L. V. E., et al. 2008, ApJ, 682, 964

Booth, C. M., & Schaye, J. 2009, MNRAS, 398, 53

Brainerd, T. G., Blandford, R. D., & Smail, I. 1996, ApJ, 466, 623

Capaccioli, M., & Schipani, P. 2011, The Messenger, 146, 2

Collett, T. E. 2015, ArXiv e-prints, arXiv:1507.02657

Conroy, C., Gunn, J. E., & White, M. 2009, ApJ, 699, 486

Conroy, C., Newman, J. A., Davis, M., et al. 2005, ApJ, 635, 982

Courteau, S., Cappellari, M., de Jong, R. S., et al. 2014, Reviews of Modern Physics, 86, 47

Crain, R. A., Schaye, J., Bower, R. G., et al. 2015, ArXiv e-prints, arXiv:1501.01311

Dalla Vecchia, C., & Schaye, J. 2012, MNRAS, 426, 140

Davis, M., Efstathiou, G., Frenk, C. S., & White, S. D. M. 1985, ApJ, 292, 371

de Jong, J. T. A., Kuijken, K., Applegate, D., et al. 2013, The Messenger, 154, 44

de Jong, J. T. A., Verdoes Kleijn, G. A., Boxhoorn, D. R., et al. 2015, ArXiv e-prints, arXiv:1507.00742

Dolag, K., Borgani, S., Murante, G., & Springel, V. 2009, MNRAS, 399, 497

Driver, S. P., Hill, D. T., Kelvin, L. S., et al. 2011, MNRAS, 413, 971

Erben, T., Hildebrandt, H., Miller, L., et al. 2013, MNRAS, 433, 2545

Ettori, S., Donnarumma, A., Pointecouteau, E., et al. 2013, Space Sci. Rev., 177, 119

Fort, B., & Mellier, Y. 1994, A&A Rev., 5, 239

Furlong, M., Bower, R. G., Theuns, T., et al. 2015, MNRAS, 450, 4486

Hoekstra, H., Yee, H. K. C., & Gladders, M. D. 2004, ApJ, 606, 67

Jiang, F., & van den Bosch, F. C. 2014, ArXiv e-prints, arXiv:1403.6827

Jing, Y. P., Mo, H. J., & Börner, G. 1998, ApJ, 494, 1

Kitching, T. D., Miller, L., Heymans, C. E., van Waerbeke, L., & Heavens, A. F. 2008, MNRAS, 390, 149

Kochanek, C. S. 1991, ApJ, 373, 354

Kuijken, K. 2011, The Messenger, 146, 8

Kuijken, K., Heymans, C., Hildebrandt, H., et al. 2015, ArXiv e-prints, arXiv:1507.00738

Mandelbaum, R., Seljak, U., Kauffmann, G., Hirata, C. M., & Brinkmann, J. 2006, MNRAS, 368, 715

Massey, R., Kitching, T., & Richard, J. 2010, Reports on Progress in Physics, 73, 086901

Melchior, P., & Viola, M. 2012, MNRAS, 424, 2757

Merson, A. I., Baugh, C. M., Helly, J. C., et al. 2013, MNRAS, 429, 556

Miller, L., Kitching, T. D., Heymans, C., Heavens, A. F., & van Waerbeke, L. 2007, MNRAS, 382, 315

Miller, L., Heymans, C., Kitching, T. D., et al. 2013, MNRAS, 429, 2858

Mitchell, P. D., Lacey, C. G., Baugh, C. M., & Cole, S. 2013, MNRAS, 435, 87

More, S., van den Bosch, F. C., Cacciato, M., et al. 2011, MNRAS, 410, 210

Moster, B. P., Naab, T., & White, S. D. M. 2013, MNRAS, 428, 3121

Peacock, J. A., & Smith, R. E. 2000, MNRAS, 318, 1144

Pforr, J., Maraston, C., & Tonini, C. 2012, MNRAS, 422, 3285

Planck Collaboration, Ade, P. A. R., Aghanim, N., et al. 2013, preprint (arXiv:1303.5076), arXiv:1303.5076

Prada, F., Vitvitska, M., Klypin, A., et al. 2003, ApJ, 598, 260

Refregier, A., Kacprzak, T., Amara, A., Bridle, S., & Rowe, B. 2012, MNRAS, 425, 1951

Robotham, A. S. G., Norberg, P., Driver, S. P., et al. 2011, MNRAS, 416, 2640

Rosas-Guevara, Y. M., Bower, R. G., Schaye, J., et al. 2013, ArXiv e-prints, arXiv:1312.0598

Schaller, M., Robertson, A., Massey, R., Bower, R. G., & Eke, V. R. 2015, ArXiv e-prints, arXiv:1505.05470

Schaye, J. 2004, ApJ, 609, 667

Schaye, J., & Dalla Vecchia, C. 2008, MNRAS, 383, 1210

Schaye, J., Crain, R. A., Bower, R. G., et al. 2015, MNRAS, 446, 521

Sifón, C., Cacciato, M., Hoekstra, H., et al. 2015, ArXiv e-prints, arXiv:1507.00737

Somerville, R. S., & Davé, R. 2014, ArXiv e-prints, arXiv:1412.2712

Springel, V. 2005, MNRAS, 364, 1105

Springel, V., White, S. D. M., Tormen, G., & Kauffmann, G. 2001, MNRAS, 328, 726

Springel, V., White, S. D. M., Jenkins, A., et al. 2005, Nature, 435, 629

Vale, A., & Ostriker, J. P. 2004, MNRAS, 353, 189

van den Bosch, F. C., Tormen, G., & Giocoli, C. 2005, MNRAS, 359, 1029

van den Bosch, F. C., Yang, X., & Mo, H. J. 2003, MNRAS, 340, 771 van Uitert, E., Cacciato, M., Hoekstra, H., & Herbonnet, R. 2015, A&A, 579, A26

van Uitert, E., Hoekstra, H., Velander, M., et al. 2011, A&A, 534, A14

Velander, M., van Uitert, E., Hoekstra, H., et al. 2014, MNRAS, 437, 2111

Viola, M., Kitching, T. D., & Joachimi, B. 2014, MNRAS, 439, 1909

Viola, M., Cacciato, M., Brouwer, M., et al. 2015, ArXiv e-prints, arXiv:1507.00735

Wiersma, R. P. C., Schaye, J., & Smith, B. D. 2009a, MNRAS, 393, 99

Wiersma, R. P. C., Schaye, J., Theuns, T., Dalla Vecchia, C., & Tornatore, L. 2009b, MNRAS, 399, 574

Wilson, G., Kaiser, N., Luppino, G. A., & Cowie, L. L. 2001, ApJ, 555, 572

Yang, X., Mo, H. J., van den Bosch, F. C., et al. 2006, MNRAS, 373, 1159

Zaritsky, D., & White, S. D. M. 1994, ApJ, 435, 599

Zehavi, I., Blanton, M. R., Frieman, J. A., et al. 2002, ApJ, 571, 172

5.A Convergence tests

In this section we report the effect on the $\Delta\Sigma$ profiles of varying the volume of the simulations keeping the resolution fixed (i.e. the initial particle masses). We make use of a simulation run in a smaller volume with respect to EAGLE, 50^3 Mpc (2×752^3 particles) instead of 100^3 Mpc (2×1504^3 particles). In this way we can isolate the effect of the size of the simulated box from the effect of changing the resolution.

Fig. 5.11 shows the $\Delta\Sigma$ profiles for all galaxies divided into 5 stellar mass bins in the range $10. < \log_{10}(M_{\rm star}[\,\mathrm{M}_\odot]) < 11.5$. We change the range relative to that used in the rest of the paper because in the smaller volume simulations there are no galaxies in the stellar mass bin $11.5 < \log_{10}(M_{\rm star}[\,\mathrm{M}_\odot]) < 11.8$. The results from the main EAGLE simulation previously employed in this work are presented by black lines whereas the $\Delta\Sigma$ profiles of the smaller volume simulations are shown by green dashed lines.

In all the stellar mass bins the $\Delta\Sigma$ profile to the left of the satellite bump is unaffected by the change in the simulated volume. The amplitude of the satellite bump is always higher in the simulations with the larger volume. This effect is due to the absence of the most massive host haloes of the 100^3 Mpc in the 50^3 Mpc volume which results in a smaller average host halo mass of satellite haloes.

We also tested the effect of varying the volume of the simulations on the satellite fraction and on the stellar mass-halo mass relation, finding very good convergence in both cases. Moreover, we report the results for the effect of resolution on the $\Delta\Sigma$ profile of all galaxies. We make use of the EAGLE simulation run on a smaller volume of 50^3 Mpc (2×752^3 particles) but with the same particle mass of the main EAGLE run, and a simulation run in the same volume 50^3 Mpc (2×376^3 particles) but with a factor of 8 decrease in mass resolution.

Fig. 5.12 shows the $\Delta\Sigma$ signal calculated in 5 stellar mass bins for all galaxies in the 50^3 Mpc volume (green curves) and for the low resolution version of the 50^3 Mpc volume (blue dotted curves). There is no clear trend with resolution apart from an increase of the overall noise of the $\Delta\Sigma$ profiles.

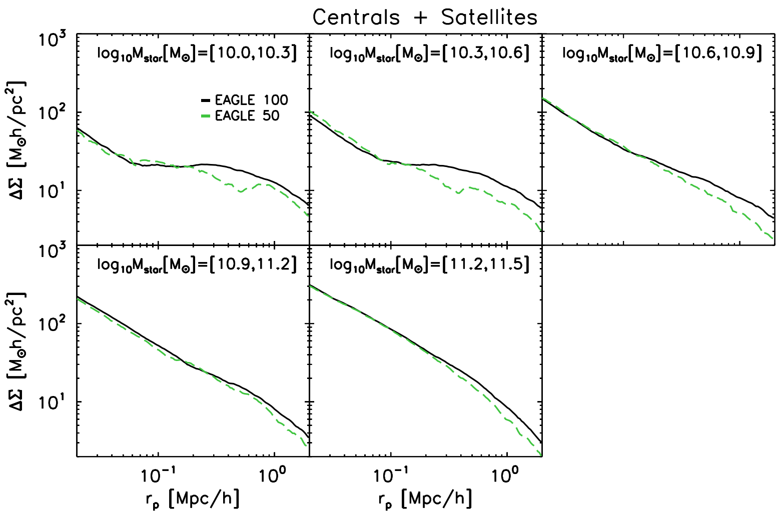

Figure 5.11: $\Delta\Sigma$ profiles for all galaxies in EAGLE (black curves) and in the smaller volume version of EAGLE run in a 50^3 Mpc volume with the same particle resolution (dashed green curves). The last stellar mass bin is missing since there are no galaxies that massive in the smaller voloume simulation.

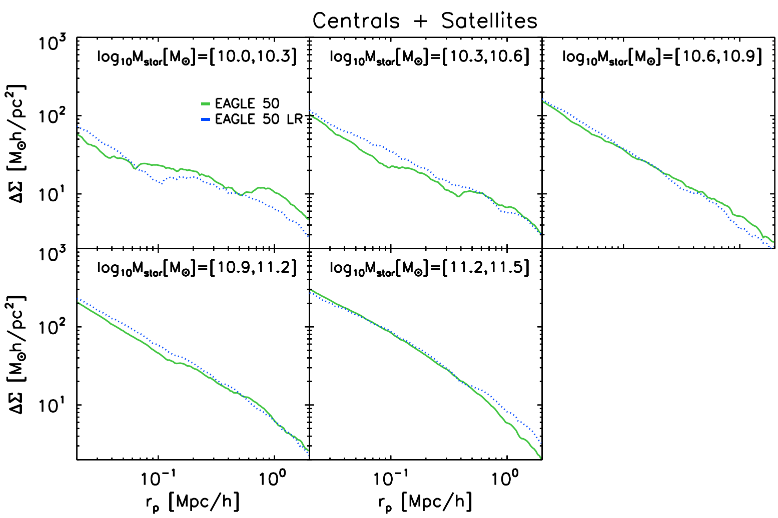

Figure 5.12: $\Delta\Sigma$ profiles for all galaxies in the smaller volume 50^3 Mpc version of EAGLE (green curves) and in the low-resolution version of the same simulation (blue dotted curves).